Research Letter **DOI:** 10.15541/jim20250113

High Temperature Resistant Calcium-doped Silica Aerogels with Enhanced Thermal Insulation *via* Sol-Gel Hydrothermal Route

LI Hao[1,2], QI Yuan[1,2], GAO Xiangdong[2], ZHANG Xingxing[2], WANG Jinmin[1]

(1. School of Materials and Chemistry, University of Shanghai for Science and Technology, Shanghai 200093, China; 2. Shanghai Institute of Ceramics, Chinese Academy of Sciences, Shanghai 200050, China)

Abstract: Silica aerogel has broad applications in the field of high-temperature thermal insulation due to its low density, low thermal conductivity and high stability. However, its thermal insulation performance deteriorates significantly at elevated temperatures exceeding 600 ℃, primarily due to the collapse of pore structure. Meanwhile, the shielding capacity of SiO_2 aerogel to the infrared radiation at high temperature is rather low due to the intrinsic properties of SiO_2. Herein, a strategy for improving the high-temperature stability and infrared shielding properties of SiO_2 aerogel *via* Ca doping was explored. Calcium-doped silica aerogel (CSA) powders were prepared by Sol-Gel, hydrothermal, and ambient pressure drying (APD) techniques using water glass and anhydrous calcium chloride as precursors and trimethylchlorosilane as a hydrophobic modifier. The effects of Ca/Si molar ratio in the precursor and hydrothermal conditions (temperature and pH) on the crystalline properties, microscopic morphology and pore structure of CSAs were investigated. The results show that the Ca/Si molar ratio and hydrothermal treatment have significant effects on the microstructure and heat resistance of CSAs in the temperature range of 400–1000 ℃. The samples sintered at 1000 ℃ have a high specific surface area of 100.1 m^2/g and a pore volume of 0.8705 cm^3/g, indicating that the CSA has good heat resistance. One-side insulation tests at temperatures up to 600 ℃ show that the sample with a Ca/Si molar ratio of 1.0 has the best insulation performance, with a cold surface temperature of 450 ℃, which is 27 ℃ lower than that of the pure silica aerogel.

Key words: silica aerogel; calcium doping; high-temperature resistance; hydrothermal; ambient pressure drying

Silica aerogel is a typical lightweight and nanoporous material with a special three-dimensional nano-network structure, well known for its extremely low density, high porosity, substantial specific surface area and low thermal conductivity at ambient temperature[1-5]. The unique and excellent properties of silica aerogels confer broad application prospects within the realms of thermal insulation, catalytic carrier, adsorption and cleaning, and biomedicine[6-9]. In special, the recent rapid industrialization of silica aerogel mats and powders around the world has significantly promoted their applications in various thermal insulation projects operating at different temperatures[10]. However, the intrinsic properties of SiO_2 pose limitations, as silica aerogel exhibits poor thermal stability at temperatures exceeding 600 ℃, as well as poor infrared shielding capacity, which largely impedes its industrial applications.

Elemental doping is an effective strategy to improve the high-temperature resistance of silica aerogels, typically achieved through formation of homogeneous composite oxide aerogels by homogeneously mixing and co-gelation of different precursors in a Sol-Gel phase[11-13]. The aerogels prepared by this method tend to have strong chemical bonds or crystalline phases that are more stable at high temperatures[14]. The more common dopant elements include aluminum, zirconium, magnesium, *etc*[15-17]. For example, Zu *et al*.[18] synthesized zirconia silica composite aerogel monolith using tetraethoxysilane and zirconium butoxide as the source materials and demonstrated good performance after heat treatment at 1000 ℃, with a high specific surface area of 172 m^2/g and a porosity of 0.97 cm^3/g.

Received date: 2025-03-18; **Revised date:** 2025-04-21; **Published online:** 2025-04-27
Biography: LI Hao (1997–), male, Master candidate. E-mail: 769718909@qq.com
李 浩(1997–), 男, 硕士研究生. E-mail: 769718909@qq.com
Corresponding author: GAO Xiangdong, professor. E-mail: xdgao@mail.sic.ac.cn; WANG Jinmin, professor. E-mail: jmwang@usst.edu.cn
高相东, 研究员. E-mail: xdgao@mail.sic.ac.cn; 王金敏, 教授. E-mail: jmwang@usst.edu.cn

Similarly, Tu *et al*.[19] prepared SiO_2/Fe_2O_3 composite aerogels based on ferric nitrate nonahydrate modified silica sol by the Sol-Gel and supercritical drying methods, achieving the low density (0.04 g/cm^3), high specific surface area (705 cm^2/g), and low thermal conductivity (0.026 W/(m·K)), thus demonstrating the potential of Fe_2O_3 in improving the thermal insulating properties of silica aerogel.

Although the calcium-doped aerogels have been used in biological and food-related applications in recent years, they are rarely reported as a means to improve the high-temperature insulation properties. Ikizler *et al*.[20] obtained calcium-silica aerogel powders using calcium chloride and sodium silicate as precursors, noting their applicability as anti-caking agents for powdered food products due to their high surface area and high water vapor adsorption capacity. Zhu *et al*.[21] reported on the calcium-doped boron nitride aerogel synthesized by reacting calcium phosphate with melamine diboronite and by introducing Ca atoms into the crystal structure of boron nitride aerogel, demonstrating high resistance to high-temperature oxidation and good thermal insulating properties.

Herein, a novel route integrating Sol-Gel, hydrothermal and APD techniques was used to fabricate CSA powders, demonstrating that calcium doping and hydrothermal treatment significantly influenced the microstructure, high temperature stability and thermal insulation of SiO_2 aerogels. The effects of Ca/Si molar ratio, hydrothermal temperature and pH were discussed in detail. The stability of CSA powders at elevated temperature up to 1000 ℃, as well as thermal insulation properties at 300–600 ℃ were examined.

1 Experimental

1.1 Materials

Industrial grade water glass (SiO_2 content 26.98%, in mass) was purchased from Yourui Refractories Co., Ltd. Anhydrous calcium chloride ($CaCl_2$, 96%, in mass) was purchased from Shanghai McLean Biochemical Technology Co., Ltd. Strongly acidic styrene cation exchange resin was purchased from Shanghai Hualing Resin Co., Ltd. Concentrated hydrochloric acid (HCl, 36.0%–38.0%, in mass) was purchased from Sinopharm Chemical Reagent Co., Ltd. Ethanol (EtOH, ≥99.7%, in mass) was purchased from Shanghai Lingfeng Chemical Reagent Co., Ltd. Trichloromethylsilane (TMCS, ≥99%, in mass) was purchased from Aladdin Biochemical Technology Co., Ltd. Cyclohexane (AR, 99.7%) was purchased from Beijing Yinuokai Science and Technology Co., Ltd.

1.2 Preparation of CSA powders

CSA powders were prepared by integrating Sol-Gel, hydrothermal and APD techniques using industrial grade water glass as silica source and anhydrous calcium chloride as calcium source, with the detailed schematic shown in Fig. 1.

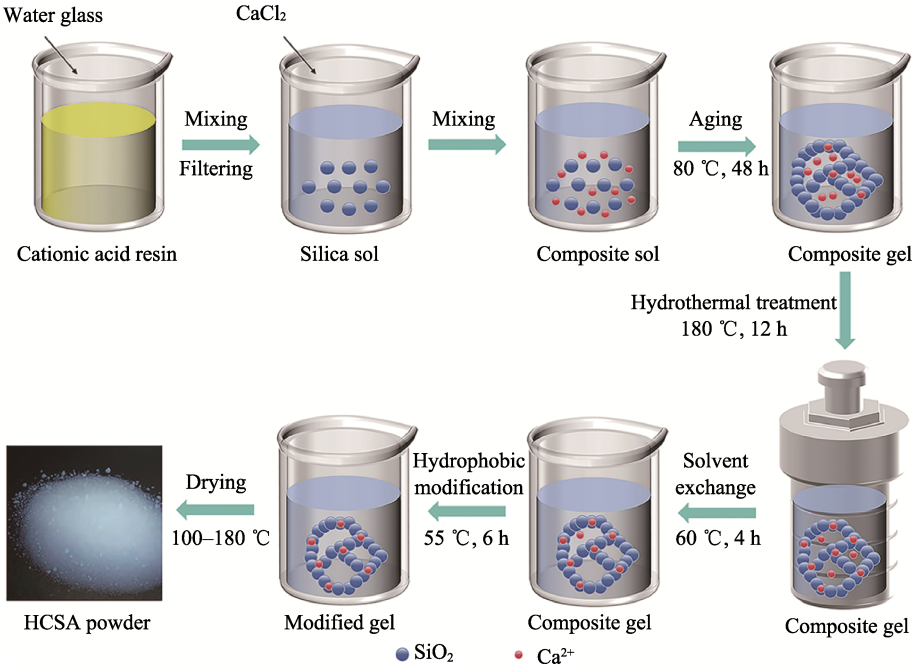

Fig. 1 Schematic illustration of the preparation process of hydrothermal CSA (HCSA) by the Sol-Gel, hydrothermal and APD method

Firstly, silica sol was prepared from industrial grade water glass *via* ion exchange using the strongly acidic styrene cation exchange resin, with a SiO_2 concentration of 26.98% (in mass). Stoichiometric amounts of calcium chloride were dissolved in silica sol with agitation to obtain a calcium-silica composite sol, with molar ratios of Ca/Si set at 0.4, 0.6, 0.8, 1.0, 1.2, and 1.5. The composite sol was gelled and aged at 80 ℃ for 48 h. Following this, the gel was mashed and transferred into a hydrothermal reactor with a certain amount of water, experiencing the hydrothermal treatment at different temperatures and pH for 12 h. After that, the gel was subjected to solvent exchange in ethanol at 60 ℃ for 4 h. Then, a mixture of cyclohexane and TMCS was added to the filter gel cake and heated at 55 ℃ for 6 h to achieve hydrophobic modification. Finally, the modified wet gel was dried at 100, 120 and 180 ℃ for 2 h, yielding the final CSA powders. The pure silica aerogel, hydrothermal pure silica aerogel, unhydrothermal CSA and hydrothermal CSA were labelled as PSA, HPSA, CSA and HCSA, respectively. When the hydrothermal conditions of the samples were not subsequently specified, the default hydrothermal temperature of 180 ℃ and the default hydrothermal pH of 5–6 were assumed. Table 1 presents the Ca/Si molar ratio and the hydrothermal condition of each sample.

1.3 Characterization

The packing density of the aerogel powder was obtained by dividing the mass of the powder by its volume after 200 vibrations on a rubber mat according to national industry standard JC/T 2518—2019. The crystallinity of the aerogels was characterized using an X-ray diffractometer (XRD, D/max 2550 V, Rigaku, Japan). The microstructure of the aerogel was characterized using scanning electron microscope (SEM, SU-9000, HITACHI, Japan) and transmission electron microscope (TEM, Tecnai G2 F20, FEI Electron Optics, Netherlands). The pore structure of the aerogels was characterized using a specific surface area and pore size analyzer (BET, Quadrasorb SI, USA). The thermal stability of the aerogels was assessed using a simultaneous thermal analyzer (TG-DSC, STA449F5, Germany). The infrared extinction capability of aerogel powders was evaluated by dispersing the samples in KBr powder at a fixed ratio (1 : 200), and subsequently placing them in a tablet pressing device for pressing, measuring and recording the weight and thickness of the tablets (1 mm). The infrared test was carried out on the platen in the range of 400–4000 cm^{-1} using a Fourier transform infrared (FTIR) spectrometer (Nicolet iS20, USA), the infrared transmittance data was recorded based on the weight and thickness of the platen. The infrared transmittance (T) and the effective specific extinction coefficient (e^*) of the sample are calculated as follows[22-26]:

$$T=I/I_0=e^{-e^*\rho s} \quad (1)$$

$$e^*=-\frac{1}{\rho s}\ln\left(\frac{I}{I_0}\right) \quad (2)$$

Where T is calculated as the ratio of the transmitted intensity (I) to the incident intensity (I_0), while e^* is determined using the thickness (s), density (ρ) and T.

Table 1 Experimental parameters of the aerogel powders

Sample	Ca/Si molar ratio	Temperature/℃	pH*
PSA	0	–	–
HPSA	0	180	5–6
CSA-0.4	0.4	–	5–6
HCSA-0.4	0.4	120	5–6
	0.4	140	5–6
	0.4	160	5–6
	0.4	180	5–6
	0.4	200	5–6
HCSA-0.6	0.6	180	5–6
HCSA-0.8	0.8	180	5–6
HCSA-1.0	1.0	180	5–6
	1.0	180	7–8
	1.0	180	9–10
	1.0	180	12–13
HCSA-1.2	1.2	180	5–6
HCSA-1.5	1.5	180	5–6

*pH was measured by the test paper prior to the hydrothermal treatment

2 Results and discussion

2.1 Effects of hydrothermal treatment and Ca/Si molar ratio

The packing density is a simple and effective indicator for evaluating the quality of aerogel powder. Effects of hydrothermal conditions and Ca/Si molar ratios on the packing density of the PSA and CSA powders were examined. The histograms of the densities of PSA and CSA under different hydrothermal conditions are shown in Fig. 2(a). The results show that the packing density of the PSA sample changes slightly after the hydrothermal treatment, regardless of the presence of water environment. In contrast, the density of CSA-0.4 increases significantly after the hydrothermal treatment with or without water, while the sample experiencing the

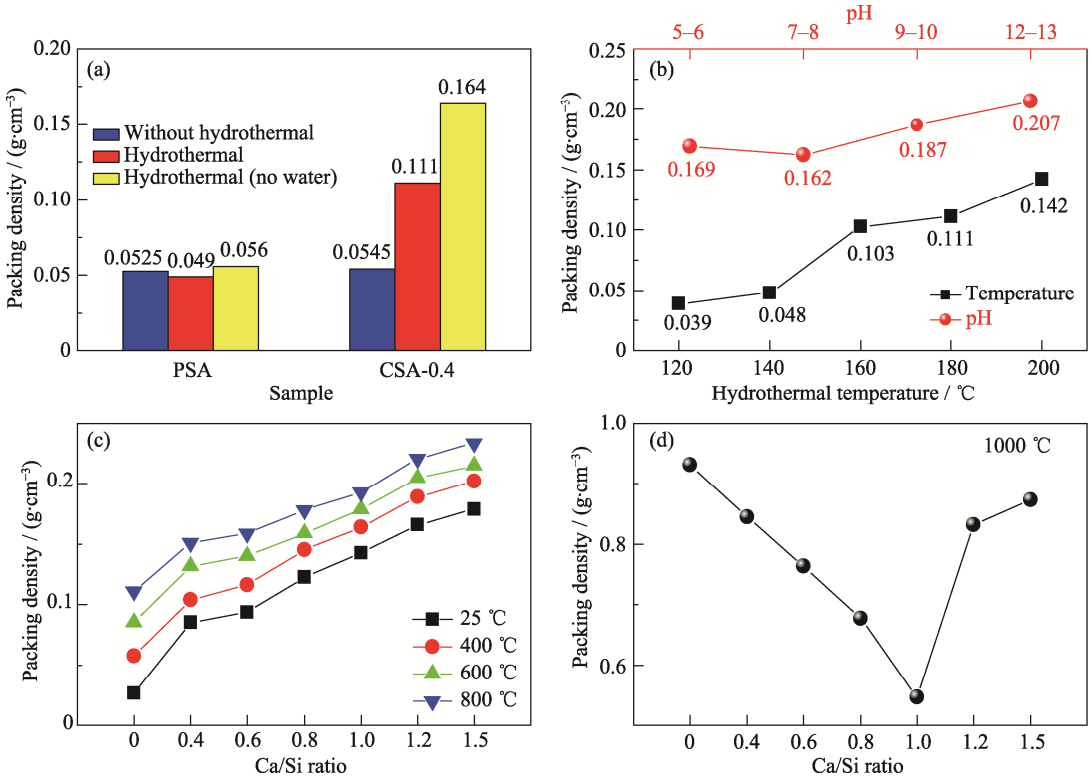

Fig. 2 Packing densities of different samples

(a) PSA and CSA-0.4 under different hydrothermal conditions; (b) HCSA-0.4 at different hydrothermal temperatures and HCSA-1.0 at different hydrothermal pH; (c, d) HCSA sintered at different temperatures for 2 h

hydrothermal treatment in water shows a lower density. This observation shows that the introduction of the calcium in the precursor can affect the surface modification and drying process, thus changing the final density of the products. Additionally, hydrothermal treatment of the Ca-Si hydrogel in an aqueous environment is more effective for obtaining the CSA with a lower density due to reduced evaporation of the water from the hydrogel compared to hydrothermal treatment without water added in the reactor.

Effects of hydrothermal temperature and pH of the aqueous environment on the density of HCSA are shown in Fig. 2(b). With the increase in hydrothermal temperature (pH is fixed at 5–6), the density of HCSA-0.4 shows an increasing trend in general. Similarly, with the increase in hydrothermal pH (temperature is fixed at 180 ℃), the density of HCSA-1.0 shows a general increasing trend. The packing density of the CSA is closely related to the degree of hydrophobic modification of SiO_2 nanoparticles, and the doping of Ca^{2+} in SiO_2 may inhibit the hydrophobic reaction facilitated by TMCS, thus reducing the packing density. Therefore, it is hypothesized that higher temperature and increased pH in the aqueous environment may promote the entering of calcium ions into the lattice of SiO_2, thus affecting the packing density. While high-quality CSA requires a low packing density and a high doping level of Ca in the lattice, selecting an appropriate hydrothermal condition is crucial.

Fig. 2(c) shows the density variation of HCSA samples with different Ca/Si molar ratios in as-prepared and sintered status. With the increase in Ca/Si molar ratio, the density of all HCSA samples exhibits a near-linear increase, with HCSA-1.5 exhibiting the highest packing density among the as-prepared samples. With the increase in sintering temperature, all HCSA samples exhibit the increasing density, with HCSA-1.5 exhibiting the highest packing density of 0.226 g/cm^3 when sintered at 800 ℃. These results indicate that a high Ca/Si molar ratio is beneficial to Ca doping, while sintering at elevated temperature may result in the partial collapse of the nanopores within CSA because of the intrinsic low softening temperature of silica (~600 ℃) and potential solid-phase sintering/diffusion driven by the high surface area and surface energy.

However, a totally different density variation trend is observed in HCSA sintered at 1000 ℃, as shown in Fig. 2(d). With the Ca/Si molar ratio ranging from 0 to 1.5, the density of sintered HCSA firstly decreases and then increases. HCSA-1.0 exhibits the lowest density of 0.547 g/cm^3. Although the large discontinuous changes suggest that the progress of solid-phase sintering at high temperatures may depend on the heating and heat conduction conditions, the non-uniformity of heat transfer

within the sample may be neglected because of the small quantity of samples (2–3 g) in a relatively large muffled oven chamber (150 mm×150 mm×150 mm). This result indicates that sintering at 1000 ℃ can significantly influence the microstructure of the HCSA, and the proper doping of calcium in SiO_2 can considerably improve the high-temperature resistance of the silica nanoporous system.

Fig. 3 presents the XRD patterns of the as-prepared PSA, HPSA, CSA-1.0 and HCSA-1.0 samples. The PSA and HPSA samples show diffusely scattered bun peaks indicative of an amorphous state. With the doping of Ca, the peaks of the samples change slightly. Following hydrothermal treatment, HCSA-1.0 shows an obviously different diffraction pattern while remaining in an amorphous state. The weak halo peak centered at 2θ= 21.6° can be identified as cristobalite (PDF#27-0605)[27]. This result shows that the doping of calcium may change the crystallization process of SiO_2 at the atomic or nanoscale level.

In order to investigate the microstructure of HCSA, SEM analyses were conducted on the as-prepared PSA, HPSA, CSA-1.0 and HCSA-1.0 samples, as shown in Figs. 4(a-d). Compared with PSA, the microscopic morphologies of HPSA, CSA-1.0 and HCSA-1.0 samples do not change significantly, presenting a three-dimensional porous skeleton network composed of nanoparticles. Energy dispersive spectrometer (EDS) analysis was performed on HCSA-1.0 samples. From the elemental mappings in Fig. 4(e) (corresponding SEM image shown in Fig. S1) and the EDS spectrum in Fig. 4(f), it can be seen that the distributions of Si, O and C are uniform in the micrometre-sized HCSA particles. The Ca content is very low (1.6% (in mass)), with slight accumulation regions. The carbon element originates from the Si–CH_3 groups anchored on the surface of SiO_2 nanoparticles. The low Ca content in the final aerogel is related to the solvent exchange, hydrothermal and hydrophobic modification processes, wherein the Ca^{2+} ions in the pores of the wet gel can diffuse into the liquid surroundings (*e.g.*, ethanol used for solvent exchange, water used for the hydrothermal treatment, and the discharging liquid during the hydrophobic modification), thus reducing the actual Ca content in the final aerogel powders. Only those Ca^{2+} ions that form strong bonds with SiO_2 are retained in the final CSA.

In order to further examine the microstructure of HCSA, the as-prepared HCSA-1.0 was analyzed by TEM, selected area electron diffraction (SAED) and high resolution transmission electron microscope (HRTEM), as shown in Fig. 5. Compared with the as-prepared HCSA-1.0, the nanoparticles of the HCSA-1.0 sample sintered at 1000 ℃ for 2 h are obviously larger (approximately tens of nanometers), but the overall nanopore structure remains unchanged. The diffraction rings become broader, and no obvious lattice fringes are detected in the HRTEM images, indicating that the nanoparticles are intrinsically amorphous. Previous studies have demonstrated pronounced agglomeration and sintering feature of pure SiO_2 aerogel after sintering at 1000 ℃[28]. In contrast, the doping of calcium in SiO_2 aerogel in present work significantly enhances the structural stability of aerogel at 1000 ℃.

2.2 Pore structure and thermal stability of HCSA

Fig. 6 shows the pore structure of HCSA-1.0 sintered at different temperatures. The adsorption-desorption

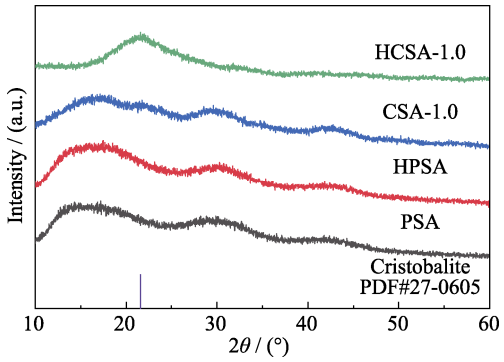

Fig. 3 XRD patterns of the PSA, HPSA, CSA-1.0, and HCSA-1.0 samples

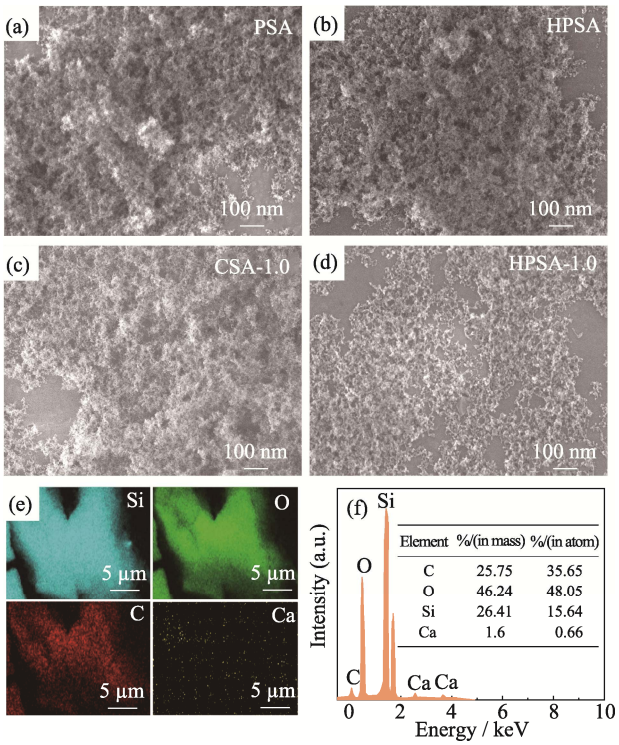

Fig. 4 (a-d) SEM images of (a) PSA, (b) HPSA, (c) CSA-1.0, and (d) HCSA-1.0; (e) Elemental mappings and (f) EDS spectrum of HCSA-1.0

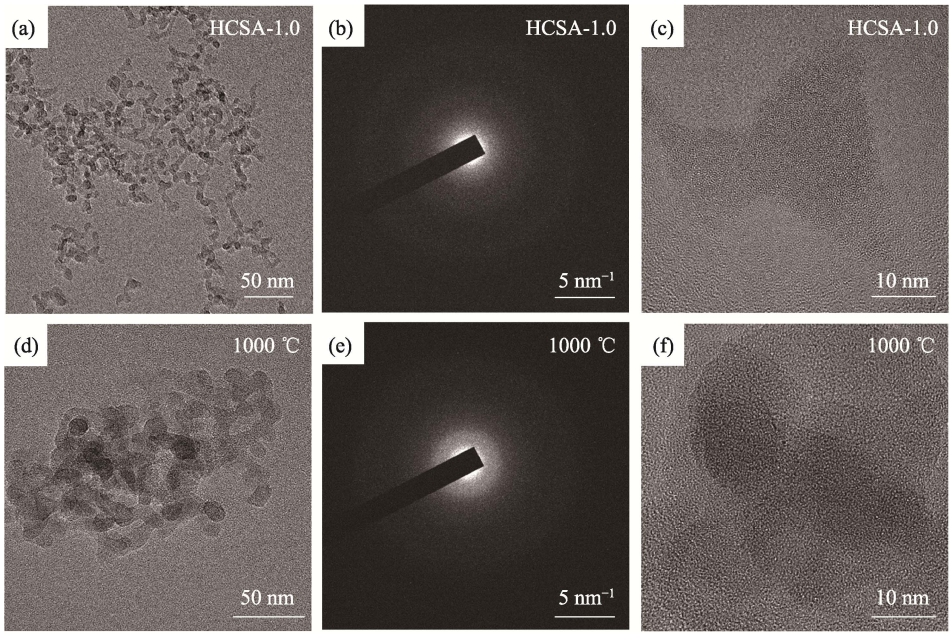

Fig. 5 (a) TEM image, (b) SAED pattern and (c) HRTEM image of the as-prepared HCSA-1.0; (d) TEM image, (e) SAED pattern and (f) HRTEM image of HCSA-1.0 sintered at 1000 ℃ for 2 h

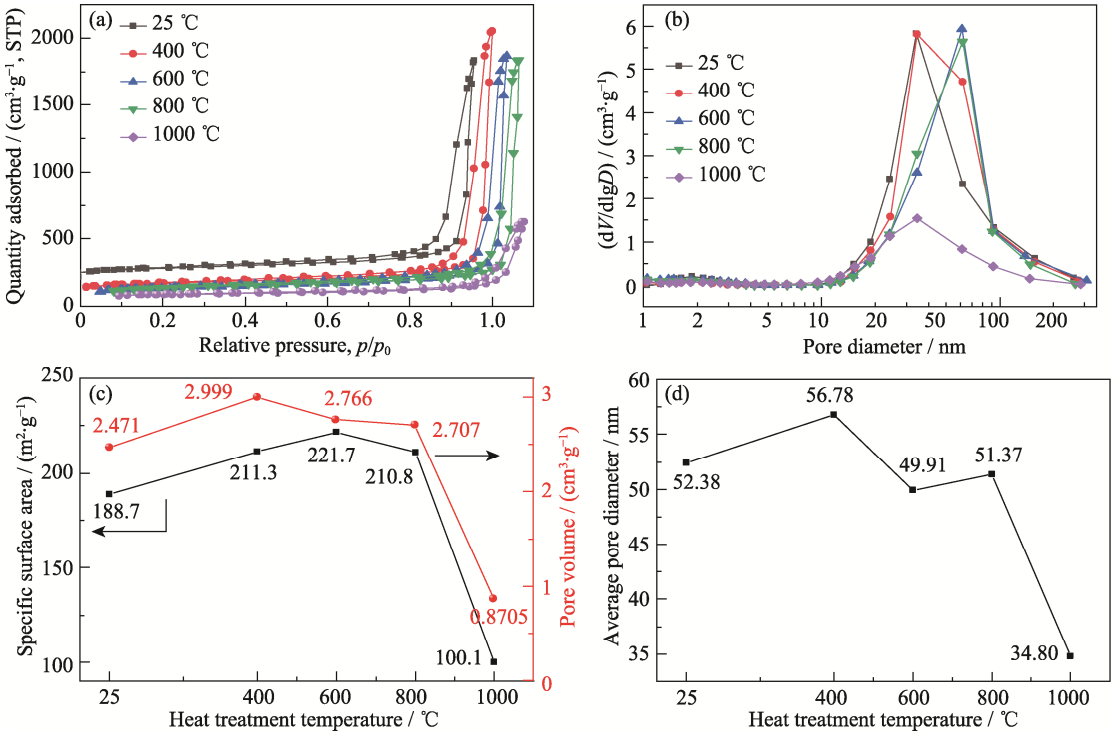

Fig. 6 Pore structure of HCSA-1.0 sintered at different temperatures
(a) Adsorption-desorption isotherms; (b) Pore size distributions (evaluated from desorption isotherm); (c) Specific surface area and pore volume; (d) Average pore size

isotherms depicted in Fig. 6(a) further elucidate the pore structure of HCSA-1.0. All samples show type IV isotherms and H3 hysteresis loops, which are characteristic of mesoporous materials. The initial portion of the isotherm rises slowly, corresponding to monolayer adsorption, while the latter portion rises sharply, indicating multilayer adsorption and capillary condensation. The presence of the H3 hysteresis loop indicates the presence of a large number of macropores in the samples, without achieving adsorption saturation[29-30]. The absorbed quantity of HCSA-1.0 reaches the maximum at 400 ℃, which is about the same at 25, 600, and 800 ℃, and decreases rapidly at 1000 ℃.

It can be seen from Fig. 6(b) that all samples exhibit a

relatively wide pore size distribution ranging from 20 to 100 nm. With the sintering temperature increasing from 400 to 600 and 800 ℃, the mode pore diameter increases correspondingly from 34 to 61 nm. However, at a sintering temperature of 1000 ℃, the sample shows a smaller mode pore size of about 34 nm than those sintered at 600 and 800 ℃.

As shown in Fig. 6(c), with the increase in sintering temperature, the specific surface area of HCSA-1.0 firstly increases and reaches the maximum value of 221.7 m^2/g at 600 ℃, then gradually decreases. When the sintering temperature rises to 1000 ℃, the specific surface area of HCSA-1.0 decreases to 100.1 m^2/g. Similarly, the pore volume firstly increases, reaching the maximum value of 2.999 cm^3/g at 400 ℃, then gradually decreases to 0.8705 cm^3/g at 1000 ℃. Sintering at 400–600 ℃ facilitates the aggregation of small particles, leading to the opening of closed pores and an increase of the pore volume. In contrast, the high-temperature calcination promotes particle consolidation, disappearance of necks, and skeleton densification, ultimately resulting in the reduction of the specific surface area and the pore volume. From Fig. 6(d), it can be seen that the average pore size of HCSA-1.0 ranges from 34.80 to 56.78 nm, which indicates that the composite aerogels maintain the nanoporous structure throughout the sintering process.

SEM images of HCSA-1.0 sintered at different temperatures are shown in Fig. 7. HCSA-1.0 sintered at 400 ℃ exhibits a well-developed porous structure with a fine three-dimensional silicon skeleton. Sintering at 600 and 800 ℃ induces slight but detectable alterations in the pore structure (as compared to Fig. 7(a)), *i.e.*, the general reduction of the nanopores. The sample sintered at 1000 ℃ displays obvious agglomeration of neighboring particles, along with a significant reduction in the quantity and size of nanopores.

Fig. S2 displays photographs of PSA and HCSA-1.0 samples sintered at 1000 ℃. After being sintered at 1000 ℃ for 2 h, the PSA sample shows significant volume shrinkage, while the HCSA-1.0 sample causes only slight shrinkage. Therefore, the HCSA-1.0 sample generally maintains the typical three-dimensional nanoporous structure, which contributes greatly to insulation at elevated temperatures. An in-depth analysis of the TEM images of HCSA-1.0 sintered at 1000 ℃ provides additional support for this observation. As shown in Fig. S3, the HCSA-1.0 sample generally maintains the typical 3D nanoporous structure, demonstrating good high temperature stability.

Fig. S4 shows the XRD patterns of HCSA-1.0 sintered at different temperatures. The samples show diffusely scattered bun peaks, indicative of their amorphous state, with no discernible change in the crystalline structure of the samples upon the increase of temperature. The obvious weak halo peak at 2θ=21.6° can be identified as cristobalite (PDF#27-0605).

Figs. 8(a, b) show the TG-DSC curves of PSA and HCSA-1.0 samples for analyzing the thermal stability of the materials and the possible physicochemical changes occurring during the sintering process. From Fig. 8(a), it is evident that the thermal weight loss of the PSA sample can

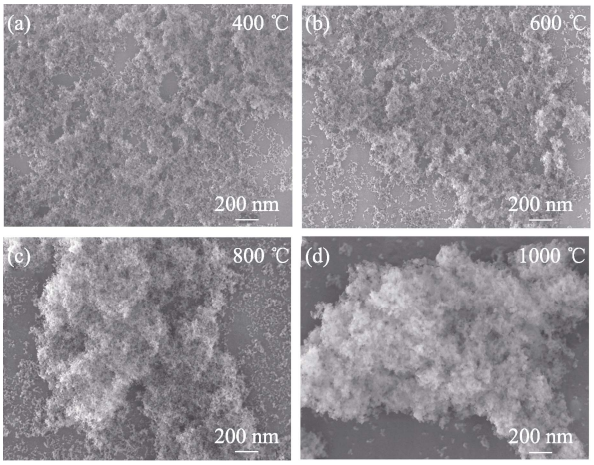

Fig. 7 SEM images of HCSA-1.0 samples sintered at (a) 400, (b) 600, (c) 800, and (d) 1000 ℃

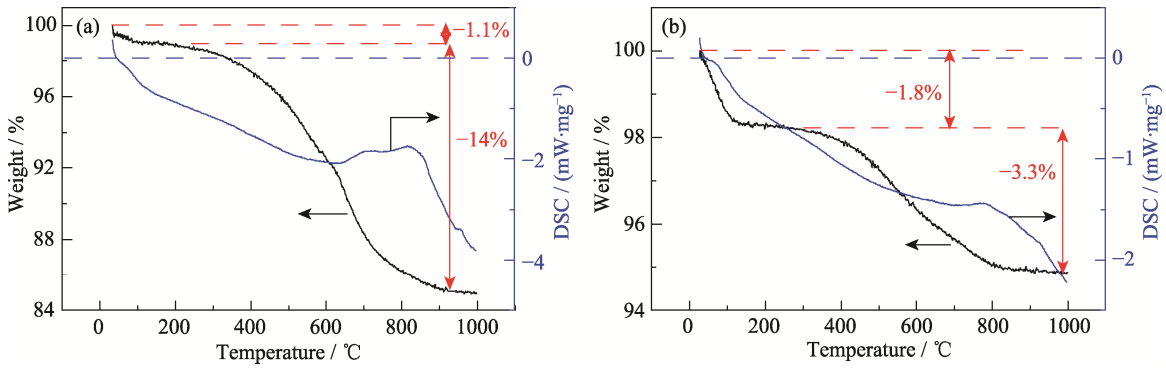

Fig. 8 TG-DSC curves of (a) PSA and (b) HCSA-1.0

be divided into two stages: the first stage (room temperature to 200 ℃), with a weight loss of 1.1%, mainly caused by the volatilization of adsorbed water and organic matter[31]; the second stage (200–1000 ℃), with a weight loss of 14%, is an exothermic process attributed to the methylene oxidation and hydroxyl condensation of silica. The total weight loss amounts to 15.5%, with two exothermic peaks at 600 and 750 ℃ in the second stage, corresponding to the formation of hydroxyl groups by methyl oxidation and the formation of Si–O–Si bonds by hydroxyl condensation, respectively[32]. Relevant reactions are provided below:

$$\equiv Si–CH_3+2O_2 \rightarrow \equiv Si–OH+H_2O\uparrow+CO_2\uparrow \quad (3)$$

$$\equiv Si–OH+HO–Si\equiv \rightarrow \equiv Si–O–Si\equiv+H_2O\uparrow \quad (4)$$

Fig. 8(b) shows that the HCSA-1.0 sample also undergoes a two-stage weight loss: the first stage (room temperature to 300 ℃), similar to that of PSA, is mainly the volatilization of adsorbed water and organics; the second stage (300–1000 ℃), with a weight loss of 3.3%, is caused by the dehydration of the skeleton (hydroxyl condensation of the neighboring silica groups). The exothermic peak at 600 ℃ disappeared with Ca doping. The total weight loss of HCSA-1.0 is 5.1%, which is significantly lower than that of PSA, indicating its improved high-temperature resistance. The much higher bond energy of Ca–O bond (3414 kJ/mol) compared to that of Si–O bond (452 kJ/mol) may be the underlying reason.

2.3 High-temperature insulation properties of HCSA powders

The high-temperature insulation properties of HCSA can be affected by many experimental factors. Up to now, no simple and effective method has been established for evaluating the thermal insulation properties of aerogel powders. Herein, an intuitive setup based on single-side heating to evaluate the insulation capacity of different aerogel powders was developed. Figs. 9(a, b) show the photo and the schematic diagram of the home-made device for measuring the thermal insulation properties for powders based on the flat heating furnace. The aerogel powders are filled into a shallow cavity with a dimension of 7.5 cm×7.0 cm×1.0 cm, which is formed by a tinplate (as the bottom) and four aerogel fiber felt bars. The top side of the aerogel powders is sealed with a tinplate of the same size. The temperature probe of paperless recorder is affixed to the tinplate using high-temperature resistant adhesive tape. A layer of fiber felt is covered on the top of the temperature probe to prevent heat loss during the test. The paperless recorder recorded the temperature changes throughout the test process.

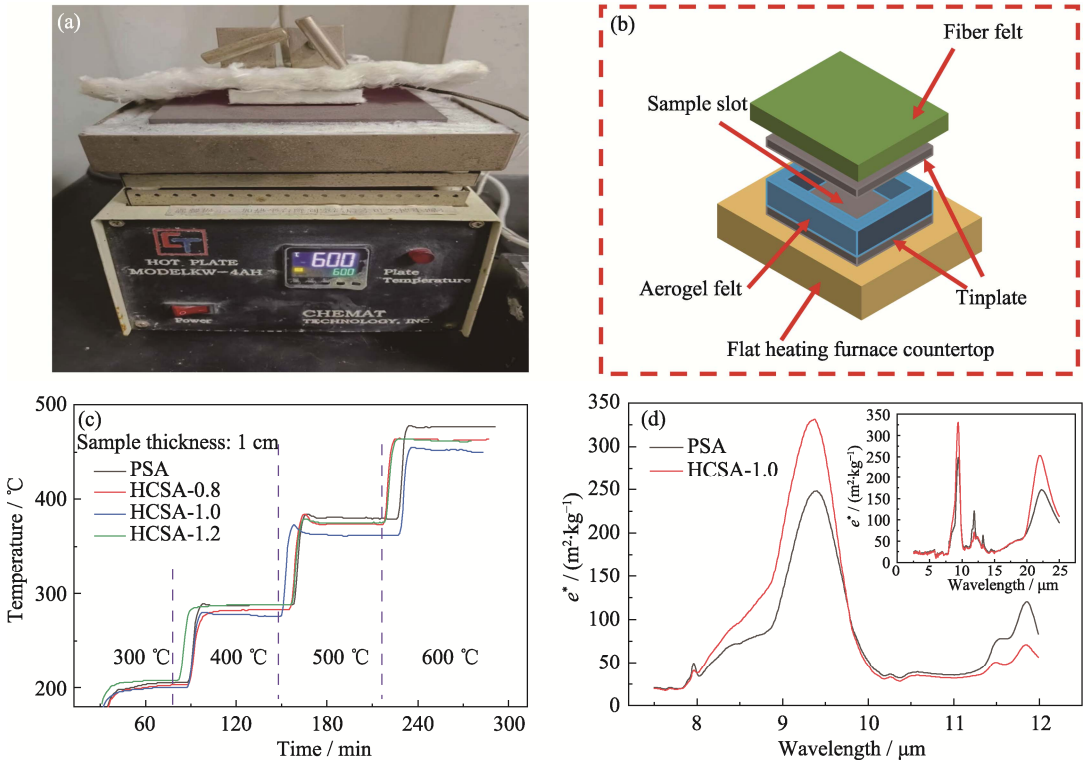

Fig. 9 (a) Flat heating furnace test device; (b) Schematic diagram of a home-made device for measuring thermal insulation properties; (c) Plots of temperature variation of the flat heating furnace test; (d) Specific extinction coefficients of PSA and HCSA-1.0 in infrared band

Colorful figures are available on website

Fig. 9(c) shows the variation of cold-surface temperature of PSA and different HCSA samples at four hot-surface temperatures of 300, 400, 500 and 600 ℃. In general, the HCSA-1.0 sample maintains a lower cold surface temperature compared to PSA and other HCSA samples. At a hot-surface temperature of 600 ℃, while PSA shows the cold-surface temperature of 477 ℃, the HCSA-1.0 sample presents the lowest cold-surface temperature of 450 ℃, which is 27 ℃ lower than that of PSA.

To further explore the underlying mechanism of the high thermal insulation of HCSA at elevated temperature, the specific extinction coefficients of PSA and HCSA-1.0 were measured, as shown in Fig. 9(d). The test was measured at room temperature. The specific extinction coefficient at room temperature may partially reflect the infrared insulation properties of the sample at elevated temperature, due to the relatively low temperature on the hot side (300–600 ℃). In the wavelength band of 8–10 μm, HCSA-1.0 exhibits obviously higher specific extinction coefficient than PSA, which may contribute to the enhanced shielding of infrared rays at high temperature, thus improving the high-temperature insulation properties. In addition, the higher specific extinction coefficient (*i.e.*, the higher absorption) in HCSA-1.0 further proves that Ca has been doped in the lattices of SiO_2, based on the direct relationship between the high absorption of SiO_2 at 8–10 μm and the enhanced asymmetry of the molecular structure due to the doping or introduction of impurities in lattice.

HCSA possesses mainly three advantages compared with other aerogels: (1) higher structural stability at high temperature up to 1000 ℃; (2) better thermal insulation at elevated temperature; (3) more functionality induced by the Ca^{2+} ions (*e.g.*, catalytic or adsorptive properties). These advantages of HCSA guarantee its wide applications in varied high-temperature insulation scenes and other areas requiring specific catalytic or adsorptive functions.

3 Conclusions

HCSA powders were prepared by integration of Sol-Gel, hydrothermal and APD techniques. The doping level of Ca^{2+} and the conditions of hydrothermal treatment affected significantly packing density, microstructure, pore structure, stability at elevated temperature (up to 1000 ℃), as well as high-temperature insulation properties at 300–600 ℃. The HCSA with a Ca/Si molar ratio of 1.0 shows a high specific surface area of 100.1 m^2/g and a pore volume of 0.8705 cm^3/g after sintering at 1000 ℃, and the lowest cold-surface temperature of 450 ℃ at the hot-surface temperature of 600 ℃. Effective doping of Ca in the SiO_2 lattice results in the effective inhibition of the condensation of hydroxyl groups during the sintering process, which may be responsible for the high stability of CSA at high temperatures.

Supporting materials

Supporting materials related to this article can be found at https://doi.org/10.15541/jim20250113.

References:

[1] AHMAD S, AHMAD S, SHEIKH J N. Silica centered aerogels as advanced functional material and their applications: a review. *Journal of Non-Crystalline Solids*, 2023, **611:** 122322.

[2] PENG F, JIANG Y, FENG J, *et al*. Research proggress on alumina aerogel composites for high-temperature thermal insulation. *Journal of Inorganic Materials*, 2021, **36(7):** 673.

[3] LI F P, CHU J B, QIU H B, *et al*. Compression resilience mechanism of silica fiber aerogel. *Journal of Inorganic Materials*, 2025, **40(9):** 981.

[4] LUO Y, XIA S, NIU B, *et al*. Preparation and high temperature inorganic transformation of flexible silicon aerogel. *Journal of Inorganic Materials*, 2022, **37(12):** 1281.

[5] AKHTER F, SOOMRO S A, INGLEZAKIS V J. Silica aerogels; a review of synthesis, applications and fabrication of hybrid composites. *Journal of Porous Materials*, 2021, **28(5):** 1387.

[6] LIU Z H, DING Y D, WANG F, *et al*. Thermal insulation material based on SiO_2 aerogel. *Construction and Building Materials*, 2016, **122:** 548.

[7] EL RASSY H, MAURY S, BUISSON P, *et al*. Hydrophobic silica aerogel-lipase biocatalysts. *Journal of Non-Crystalline Solids*, 2004, **350:** 23.

[8] RAO A V, HEGDE N D, HIRASHIMA H. Absorption and desorption of organic liquids in elastic superhydrophobic silica aerogels. *Journal of Colloid and Interface Science*, 2007, **305(1):** 124.

[9] MALEKI H, DURAES L, GARCIA-GONZALEZ C A, *et al*. Synthesis and biomedical applications of aerogels: possibilities and challenges. *Advances in Colloid and Interface Science*, 2016, **236:** 1.

[10] LAMY-MENDES A, PONTINHA A D R, ALVES P, *et al*. Progress in silica aerogel-containing materials for buildings' thermal insulation. *Construction and Building Materials*, 2021, **286:** 122815.

[11] ALMEIDA C M R, GHICA M E, DURÃES L. An overview on alumina-silica-based aerogels. *Advances in Colloid and Interface Science*, 2020, **282:** 102189.

[12] WALKER R C, POTOCHNIAK A E, HYER A P, *et al*. Zirconia

aerogels for thermal management: review of synthesis, processing, and properties information architecture. *Advances in Colloid and Interface Science*, 2021, **295:** 102464.

[13] KIM Y N, SHAO G N, JEON S J, *et al*. Sol-Gel synthesis of sodium silicate and titanium oxychloride based TiO_2-SiO_2 aerogels and their photocatalytic property under UV irradiation. *Chemical Engineering Journal*, 2013, **231:** 502.

[14] GAO S, YANG T, LIU S N, *et al*. Preparation of high-temperature resistant aluminum-doped silica aerogel from aluminum sol source by ambient pressure drying. *Journal of Sol-Gel Science and Technology*, 2023, **109(1):** 162.

[15] WU Y, WANG X D, SHEN J. Metal oxide aerogels for high-temperature applications. *Journal of Sol-Gel Science and Technology*, 2022, **106(2):** 360.

[16] GAO S, CAO Z Q, LIU K, *et al*. Preparation of high-temperature resistant aerogels by incorporating aluminum sol into composite silica sources using ambient pressure drying. *Polymers*, 2024, **16(16):** 2296.

[17] ZHANG X X, GAO X D, DONG Y B, *et al*. Nanoporous Mg-doped SiO_2 nanoparticles with tunable infrared emissivity toward effective radiative cooling coatings. *Journal of Alloys and Compounds*, 2023, **940:** 168905.

[18] ZU G Q, SHEN J, ZOU L P, *et al*. Highly thermally stable zirconia/silica composite aerogels prepared by supercritical deposition. *Microporous and Mesoporous Materials*, 2017, **238:** 90.

[19] TU F, YU Y X, WANG Y, *et al*. Preparation of SiO_2/Fe_2O_3 composite aerogels for thermal insulation enhancement. *Ceramics International*, 2024, **50(2):** 2976.

[20] IKIZLER B K, YAPC E, YÜCEL S, *et al*. Production and characterization of calcium silica aerogel powder as a food additive. *ACS Omega*, 2023, **8(12):** 11479.

[21] ZHU M Y, LI G Y, GONG W B, *et al*. Calcium-doped boron nitride aerogel enables infrared stealth at high temperature up to 1300 ℃. *Nano-Micro Letters*, 2021, **14(1):** 18.

[22] YANG J X, ZHANG Y W, HONG Z L, *et al*. Preparations of TiO_2 nanocrystal coating layers with various morphologies on mullite fibers for infrared opacifier application. *Thin Solid Films*, 2012, **520(7):** 2651.

[23] FENG J P, CHEN D P, NI W, *et al*. Study of IR absorption properties of fumed silica-opacifier composites. *Journal of Non-Crystalline Solids*, 2010, **356(9/10):** 480.

[24] WANG X D, SUN D, DUAN Y Y, *et al*. Radiative characteristics of opacifier-loaded silica aerogel composites. *Journal of Non-Crystalline Solids*, 2013, **375:** 31.

[25] WEI G S, LIU Y S, ZHANG X X, *et al*. Thermal conductivities study on silica aerogel and its composite insulation materials. *International Journal of Heat and Mass Transfer*, 2011, **54(11/12):** 2355.

[26] YOU J G, XING H P, XUE J, *et al*. Preparation of rigid cross-linked PVC foam with excellent thermal insulation through adding high-reflectivity IR opacifier. *Composites Science and Technology*, 2021, **203:** 108566.

[27] SHI T Q, GAO X D, WU Y Q, *et al*. Ba/Sn induced high temperature phase and microstructure evolution of silica aerogel *via* co-precursor Sol-Gel method. *Chemical Physics*, 2021, **545:** 111161.

[28] YAO J Q, GAO X D, WU Y Q, *et al*. High-temperature resistant ambient pressure-dried aluminum doped silica aerogel from inorganic silicon and aluminum sources. *Ceramics International*, 2022, **48(11):** 15006.

[29] SING K S W. Reporting physisorption data for gas/solid systems with special reference to the determination of surface area and porosity. *Pure and Applied Chemistry*, 1985, **57(4):** 603.

[30] ROUQUEROL J, AVNIR D, FAIRBRIDGE C W, *et al*. Recommendations for the characterization of porous solids. *Pure and Applied Chemistry*, 1994, **66(8):** 1739.

[31] BHAGAT S D, RAO A V. Surface chemical modification of TEOS based silica aerogels synthesized by two step (acid-base) Sol-Gel process. *Applied Surface Science*, 2006, **252(12):** 4289.

[32] BHAGAT S D, KIM Y H, AHN Y S, *et al*. Rapid synthesis of water-glass based aerogels by *in situ* surface modification of the hydrogels. *Applied Surface Science*, 2007, **253(6):** 3231.

溶胶凝胶水热法制备耐高温、隔热增强钙掺杂二氧化硅气凝胶

李 浩[1,2], 齐 源[1,2], 高相东[2], 张星星[2], 王金敏[1]

(1. 上海理工大学 材料与化学学院, 上海 200093; 2. 中国科学院 上海硅酸盐研究所, 上海 200050)

摘 要: 二氧化硅气凝胶因低密度、低导热系数和良好的高温稳定性, 广泛应用于高温隔热领域, 但由于其固有的材料特性, 当工作温度超过 600 ℃, 其孔结构将逐渐塌缩, 从而使隔热性能大幅度衰减, 同时在高温下红外辐射的遮蔽效果也较差。本研究旨在探讨通过钙掺杂提高二氧化硅气凝胶的高温稳定性及红外遮蔽能力。以水玻璃和无水氯化钙为前驱体, 以三甲基氯硅烷(TMCS)为疏水改性剂, 通过溶胶-凝胶、水热和常压干燥(APD)技术制备了耐高温的钙掺杂二氧化硅气凝胶(CSA)粉体。研究了前驱体中 Ca/Si 摩尔比和水热条件(温度和 pH)对 CSA 结晶特性、微观形貌和孔结构的影响。结果表明, 在 400~1000 ℃范围内, Ca/Si 摩尔比和水热处理对 CSA 的微观结构和耐热性有显著影响。1000 ℃烧结的样品具有较高的比表面积(100.1 m^2/g)和孔容(0.8705 cm^3/g), 表明 CSA 具有良好的耐高温性能。温度高达 600 ℃的单面隔热测试表明, Ca/Si 摩尔比为 1 的样品隔热性能最好, 冷表面温度为 450 ℃, 比纯二氧化硅气凝胶低 27 ℃。

关 键 词: 二氧化硅气凝胶; 钙掺杂; 耐高温性; 水热; 常压干燥

中图分类号: TQ424 **文献标志码:** A **文章编号:** 1000-324X(2026)02-0262-11

Supporting Materials:

High Temperature Resistant Calcium-doped Silica Aerogels with Enhanced Thermal Insulation *via* Sol-Gel Hydrothermal Route

LI Hao[1,2], QI Yuan[1,2], GAO Xiangdong[2], ZHANG Xingxing[2], WANG Jinmin[1]

(1. School of Materials and Chemistry, University of Shanghai for Science and Technology, Shanghai 200093, China; 2. Shanghai Institute of Ceramics, Chinese Academy of Sciences, Shanghai 200050, China)

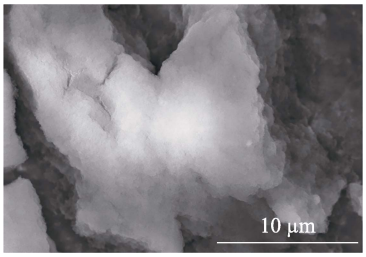

Fig. S1 Low resolution SEM image used for EDS mapping test

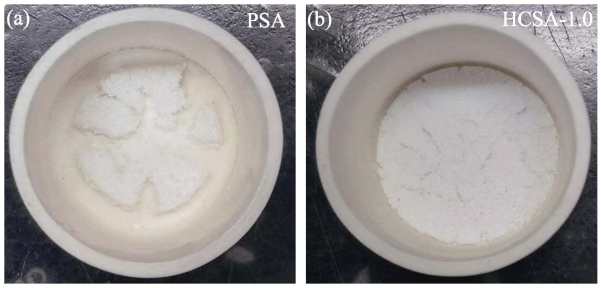

Fig. S2 Photographs of PSA (a) and HCSA-1.0 (b) samples calcined at 1000 ℃

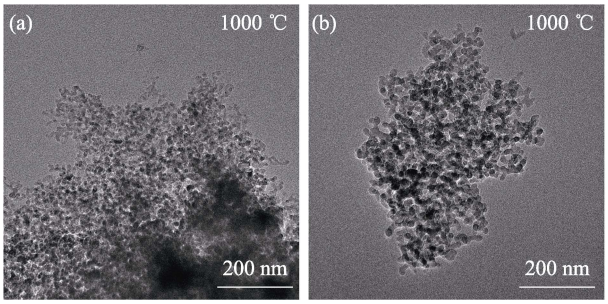

Fig. S3 TEM images of HCSA-1.0 calcined at 1000 ℃
(a) Fringe of a large particle; (b) A small particle

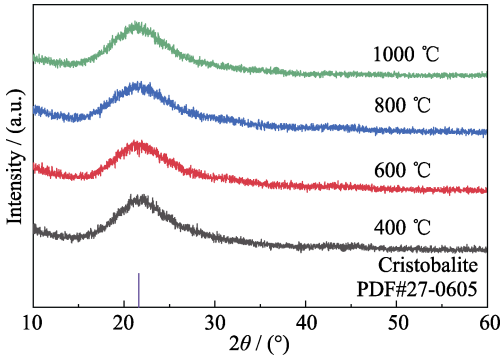

Fig. S4 XRD patterns of HCSA-1.0 sintered at different temperatures